

# Global dissociation of the amygdala from the rest of the brain during REM sleep

**Marta Matei**

INSERM/ESPCI PSL Paris/CNRS

**Antoine Bergel**

Physics for Medicine Institute, Inserm U1273, CNRS UMR 8063, ESPCI Paris, PSL Research University

<https://orcid.org/0000-0002-3011-205X>

**Sophie Pezet**

ESPCI Paris <https://orcid.org/0000-0002-3305-3315>

**Mickael Tanter** (✉ [mickael.tanter@espci.fr](mailto:mickael.tanter@espci.fr))

INSERM/ESPCI PSL Paris /CNRS <https://orcid.org/0000-0001-7739-8051>

---

## Article

**Keywords:** REM sleep, Brain hemodynamics, Neurovascular coupling, Ultrasound imaging, Theta rhythm, Gamma rhythms

**Posted Date:** December 3rd, 2021

**DOI:** <https://doi.org/10.21203/rs.3.rs-1107674/v1>

**License:** © ⓘ This work is licensed under a Creative Commons Attribution 4.0 International License.

[Read Full License](#)

---



18 **Abstract**

19 Rapid-eye-movement sleep (REMS) or paradoxical sleep is associated with intense neuronal  
20 activity, fluctuations in autonomic control, body paralysis and brain-wide hyperemia. The  
21 mechanisms and functions of these energy-demanding patterns remain elusive and a global  
22 picture of brain activation during REMS is currently missing. In the present work, we performed  
23 functional ultrasound (fUS) imaging at the whole-brain scale during hundreds of REMS  
24 episodes to provide the spatiotemporal dynamics of vascular activity in 259 brain regions  
25 spanning more than 2/3 of the total brain volume. We first demonstrate a dissociation between  
26 basal/midbrain and cortical structures, the first ones sustaining tonic activation during REMS  
27 while the others are activated in phasic bouts. Second, we isolated the vascular compartment  
28 in our recordings and identified arteries in the anterior part of the brain as strongly involved in  
29 the blood supply during REMS episodes. Finally, we report a peculiar activation pattern in the  
30 amygdala, which is strikingly disconnected from the rest of the brain during most but not all  
31 REMS episodes. This last finding shows that amygdala undergoes specific processing during  
32 REMS and may be linked to the regulation of emotions and the creation of dream content  
33 during this very state.

34  
35 195 words

## 36 **Introduction**

37

38 Several studies have shown a strong link between REM sleep (REMS) and emotions.  
39 According to Gujar and colleagues, REMS is strongly linked to the recalibration of the human  
40 brain's reactivity towards specific emotions with a decreased reactivity towards fearful memory  
41 but a significant enhancement toward happy memories (Gujar et al., 2011). Moreover, several  
42 studies tend to show that the emotional memories are better recalled than neutral memories  
43 (Phelps, 2004) especially during REM-rich sleep (Groch et al., 2015; Nishida et al., 2009;  
44 Wagner et al., 2001). It is also now well established that REMS disturbances are often  
45 observed in PTSD cases. Mellman and colleagues have observed shorter and more frequent  
46 sleep bouts in trauma-exposed patients compared to non-injured ones (Mellman et al., 2002).  
47 These findings were later confirmed, as well as other observations stating that REMS  
48 disturbances led to impaired fear extinction learning, which might explain the development and  
49 maintenance of PTSD symptoms (Bottary et al., 2020; Pace-Schott et al., 2015; Spoomaker,  
50 2018). A "sleep to forget, sleep to remember" (SFSR) model arose a few years ago, which  
51 divides the memories in two parts: the factual memory (the actual event), and its emotional  
52 part (the feelings and their intensity from the event) (Walker and van der Helm, 2009). The  
53 former is consolidated during REMS, while the latter is de-potentiated, meaning that the factual  
54 memory remains embedded in the hippocampus, while the intensity of the feelings attached to  
55 this memory is downscaled. This is considered as an "overnight therapy", necessary to cope  
56 with distressful events and which is disturbed in cases of emotion-based disorders, such as  
57 depression or posttraumatic stress disorder (PTSD), as these disorders are often linked with  
58 REMS disturbances as previously stated. However, a few studies go against that model  
59 (Wiesner et al., 2015). The biological mechanisms of emotional regulation of memories involve  
60 an amygdala-hippocampal-medial prefrontal cortical (mPFC) network, whose  
61 intercommunications are enhanced by theta and ponto-geniculo-occipital (PGO) oscillations  
62 (or equivalent P-wave in rats), as well as elevated acetylcholine and cortisol levels during  
63 REMS (Hutchison and Rathore, 2015; van der Helm et al., 2011).

64 In addition to the regulation and processing of emotions, several other functions have been  
65 attributed to REMS, such as, for example, memory consolidation (which depends upon the  
66 hippocampal theta oscillations created by activation of GABAergic neurons in the medial  
67 septum (Boyce et al., 2016)), or the brain maturation specifically during early life REMS (Marks  
68 et al., 1995) and more precisely to aid sensorimotor system development through muscle  
69 twitches (Blumberg et al., 2013). Another function attributed to REMS is that of forgetting

70 memories (see (Langille, 2019) for a review) probably through the activation of melanin-  
71 concentrating-hormone (MCH)-producing neurons (Izawa et al., 2019).

72 From a physiological point of view, complex brain circuits have been shown to play a role in  
73 REMS. For example, in the brainstem (Sastre and Jouvet, 1979), two subsets of glutamatergic  
74 neurons (so called REM-on neurons) located in the latero-dorsal tegmental area (LDT) and in  
75 the sub-latero-dorsal tegmental nucleus (SLD) have been described: the first one projecting to  
76 the forebrain, responsible for the generation of hippocampal theta rhythm and desynchronized  
77 cortical activity, the second one projecting to the brainstem and responsible for muscle atonia  
78 hence the suppression of motor activity (Peever and Fuller, 2017). Furthermore, the melanin  
79 concentrating hormone (MCH), known to play a role in the promotion of REMS, is synthesized  
80 by neurons in the hypothalamus (Vetrivelan et al., 2016). However, the downstream activations  
81 of these pathways are completely unknown. Taken together, these examples show that REMS  
82 is a complex brain state which involves many brain regions scattered across the brain,  
83 rendering the global investigation of REMS challenging. Apart from the hippocampal structure  
84 (Grosmark et al., 2012; Montgomery et al., 2008; Popa et al., 2010), a clear whole-brain  
85 electrophysiological characterization of REMS is currently missing. Though some fMRI/PET  
86 studies have investigated functional connectivity associated with REMS (Chow et al., 2013;  
87 Wehrle et al., 2007), the limited temporal resolution and complexity of these techniques  
88 impedes the characterization of whole-brain networks during single REMS episodes. Hence,  
89 a clear picture of global brain activity during REMS is missing.

90 Interestingly, a recent study using functional ultrasound (fUS) coupled to LFP recordings in  
91 rats, uncovered an intense hyperemic activity largely exceeding both NREMS and wake levels  
92 (Bergel et al., 2018). These large-amplitude hyperemic patterns in the hippocampus, thalamus  
93 and cortex occurred in phasic bouts, followed a sequential thalamus-hippocampus-temporal  
94 cortex pattern and were robustly preceded by fast-gamma oscillations in the CA1 region. Such  
95 intense hyperemic activity were also imaged using functional ultrasound in human neonates  
96 during active sleep (Demene et al., 2017). Another recent study confirmed this hyperemic  
97 activity during REMS, using intrinsic optical imaging (ISOI) in sleeping head-fixed mice (Turner  
98 et al., 2020). Notably, these findings are in line with the entrainment of arteriole diameter by  
99 gamma activity in the cortex of head-fixed mice during wake (Mateo et al., 2017). In both  
100 studies, the characterization of neurovascular interactions was restricted to the cortex. This is  
101 striking, as sleep is generally thought to be a period when the body is resting and its energy  
102 restored (Cirelli and Tononi, 2008; Schmidt, 2014; Siegel, 2005), yet this hyperemic activity  
103 seems to be extremely energy consuming. We assume that if such energy-demanding activity

104 has been maintained across evolution, it must have some important role for the survival of the  
105 animal, which does not seem to have been found yet.

106 As previous studies could not give a global view of REMS's brain activity, we took advantage  
107 of fUS versatility to scan more than 250 brain regions over multiple coronal and sagittal planes  
108 during more than 600 REM episodes. This study thus provides an exhaustive characterization  
109 of global brain hemodynamics during rodent REMS. We demonstrate a clear dissociation  
110 between basal/midbrain structures and superficial ones, respectively activated in a tonic and  
111 phasic manner. We also disentangle the vascular structures involved in the irrigation of the  
112 brain during REMS episodes providing a detailed outlook of blood supply. Finally, we show  
113 that brain activity reveals a striking dissociation between the amygdala complex and the rest  
114 of the brain regions.

115

## 116 **Results**

117 This study aimed at investigating the large-scale hemodynamics during REMS, in particular in  
118 the amygdalar network. Using a chronic experimental approach developed previously (Sieu et  
119 al., 2015), which included a cranial window and the implantation of a permanent fUS-  
120 compatible plastic prosthetic skull, that also enabled the attachment of the ultrasound probe  
121 holder (Figure 1A). In this setup, the different regions of the brain were monitored in a series  
122 of coronal and sagittal planes, each acquisition lasting 30 minutes for 4-6h per day over the  
123 course of several days (Figure 1B). This resulted in a dataset of 84 recordings in n=8 animals,  
124 totalizing 617 REM episodes recorded in 259 brain regions (Supplementary Figure S2),  
125 together with hippocampal local field potentials (LFP) recordings, accelerometer, and neck  
126 electromyogram (EMG) (Figure 1C, Supplementary Table 1).

### 127 ***Distribution of CBV changes across brain regions during diverse arousal states***

128 Measurement of the CBV in n=3 rats, in a total of 72 recordings, in which the animal is  
129 spontaneously going through different arousal states (quiet wake - QW, active wake - AW,  
130 non-REM sleep - NREMS, REM sleep - REMS) revealed a quiescent level of CBV fluctuations  
131 in QW and NREMS (Figure 2A). AW however is associated with increased cortical CBV levels  
132 especially in the primary sensory areas, while REMS is characterized by increased CBV in all  
133 brain regions with strongest effect in the hippocampal and limbic structures.

134 As we aimed at studying in detail the hemodynamic changes in various parts of the brain during  
135 REMS, we next focused on the changes in a large number of regions of interests located under

136 our various imaging planes, by computing the percentage of CBV change during REMS.  
137 Calculations were performed using 1-3 min of either the QW or the AW for the baseline (Figure  
138 2B). This double analysis shows consistently a large range of CBV changes in association with  
139 REM between different parts of the brain in both analyses. While the hippocampal formation,  
140 the periaqueductal grey (PAG), the superior colliculus (SC) and some parts of the cortex, (such  
141 as the cingulate and retrosplenial cortices) present a strong percentage of CBV increase during  
142 REMS, areas of the hypothalamus and laterally located cortices (auditory, rhinal, piriform  
143 cortices) present modest CBV increases during REMS (Figure 2B). This combined analysis  
144 demonstrates that REMS hyperemia is not only a state of intense activation with respect to  
145 QW and NREMS, which are known to quiescent states, but also to AW in all brain regions,  
146 with strongest effects in the hippocampus and midbrain structures. Detailed mean values of  
147 the CBV distributions in all regions across the different vigilance states are details in  
148 Supplementary Tables 2 & 3.

149

### 150 ***Dissociation between the basal brain and the superficial brain areas during tonic and*** 151 ***phasic activations***

152 We previously described strong hemodynamic changes, composed of both phasic and tonic  
153 components (Bergel et al., 2018). By thresholding vascular activity during REMS, we were  
154 able to extract a binary variable that accounted for the phasic component of REMS (seed  
155 phasic-REM, equals 2 during phasic activity, 1 during REM, 0 otherwise), that we used as a  
156 'seed' for correlation analyses and compared it with another variable accounting for the tonic  
157 component of REMS (seed REM, equals 1 during REMS, 0 otherwise) (Figure 3A). Individual  
158 voxels taken in the superficial or deep structures of the brain show different activation profiles,  
159 voxels in basal brain structures showing a very tonic activation (sustained during a single  
160 REMS episode) while superficial pixels were active intermittently by phasic bouts, which was  
161 captured by the different cross-correlations functions obtained with seed-phasic REM and  
162 seed-REM (Figure 3B). This phenomenon was clearly visible on all correlation maps (each  
163 pixel displays the maximum of the cross-correlation function shown in 3B) generated with  
164 either seed: cortical structures were more strongly associated with REMS-phasic than with  
165 REMS (black arrows) on all brain sections (Figure 3C). This effect was confirmed in regional  
166 analysis across individuals and interestingly the timing associated with either seed variable  
167 yielded different information. Interestingly, timings associated with seed-REM captured the  
168 broad inter-episode fluctuations while those associated with REM phasic, revealed a precise  
169 sequence of activation between brain regions and captured the intra-REM fluctuations (Figure  
170 3D). Moreover, a few brain regions stand out with very high correlation scores such as the

171 substantia nigra (SNi) ( $R_{\max \text{ phasic}} = 0.7702 \pm 0.0204$ ,  $R_{\max} = 0.7115 \pm 0.0173$ ,  $N=3$  animals), the  
172 dorsal periaqueductal grey (dPAG) ( $R_{\max \text{ phasic}} = 0.8111 \pm 0.0277$ ,  $R_{\max} = 0.7408 \pm 0.0228$ ,  $N=3$   
173 animals), the superior colliculus (SC) ( $R_{\max \text{ phasic}} = 0.7706 \pm 0.0313$ ,  $R_{\max} = 0.6967 \pm 0.0340$ ,  
174  $N=3$  animals), the pretectal nuclei (PN) ( $R_{\max \text{ phasic}} = 0.7834 \pm 0.0398$ ,  $R_{\max} = 0.6667 \pm 0.0384$ ,  
175  $N=3$  animals) and preoptic area (POA) ( $R_{\max \text{ phasic}} = 0.7164 \pm 0.0240$ ,  $R_{\max} = 0.6803 \pm 0.0223$ ,  
176  $N=3$  animals), as was seen in Figure 2B. In both analyses however, all cortical regions, except  
177 parietal ( $R_{\max \text{ phasic}} = 0.5493 \pm 0.0260$ ,  $R_{\max} = 0.4708 \pm 0.0265$ ,  $N=3$  animals) and retrosplenial  
178 ( $R_{\max \text{ phasic}} = 0.6607 \pm 0.0315$ ,  $R_{\max} = 0.5841 \pm 0.0272$ ,  $N=3$  animals) cortices and all amygdala  
179 subregions (basal, lateral, cortical and residual amygdala) displayed lower correlation  
180 coefficients than other brain structures (Supplementary Table 4).

181

### 182 ***Selective contribution of vascular dynamics to the blood supply during REM sleep***

183 The second major aim of this study was to elucidate the contribution of the vascular  
184 compartment. We first segmented all salient vascular structures in our imaging planes  
185 including parallel branches of the main cerebral arteries (anterior cerebral artery - acer, anterior  
186 choroidal artery - ach, middle cerebral artery - mcer, and posterior cerebral artery - pcer) and  
187 segments along on the anterior branch (anterior cerebral artery - acer, azygos of anterior  
188 cerebral artery - azac, azygos pericallosal artery - azp) (Figure 4A-B). We then investigated  
189 the temporal dynamics in these structures by re-aligning their time course to the start of each  
190 REMS episode (defined by hippocampal theta activity crossing a threshold) and averaged their  
191 activation profile, both from the onset and of REMS (Figure 4C-D and E-F). Quantifications  
192 show an increased CBV (expressed in percentage of variation relative to the QW baseline) at  
193 the beginning of REMS, a sustained level throughout the REM episode and finally a sudden  
194 drop at the end of the REM episode. This increased CBV in arteries was more pronounced (2-  
195 fold increase) in the arteries that vascularize the rostral part of the brain (acer, azac and azp),  
196 compared to the arteries that vascularize the medial and posterior parts of the brain (ach, mcer,  
197 pcer), confirming a general phenomenon of increased blood supply during REMS, but also an  
198 emphasis of this enhanced blood flow in the rostral part of the brain. Further analysis shows a  
199 significant propagation delay along the anterior branch with acer peaking earlier than azac and  
200 azp (acer:  $t_1 = -3.14 \pm 3.26$ s, azac:  $t_1 = 1.73 \pm 6.50$ s, azp:  $t_1 = 1.81 \pm 3.03$ s) (Figure 4G)  
201 Such REM-associated increased CBV was observed at a lower level in veins with a surprising  
202 antagonist activity between two side-by-side veins: the longitudinal hippocampal vein (lhiv) and  
203 the azygos internal cerebral vein (azicv) (Supplementary Figure S3).

204

### 205 ***Atypical amygdala activity during REM sleep***

206 When assessing inter-regional correlations in the CBV signal, the most striking pattern of  
207 activity was found in the amygdala and consisted of a robust disconnection from the rest of the  
208 brain, which was clearly visible on ‘functional connectivity’ matrices averaged over all REMS  
209 episodes (Figure 5A) and in the temporal fluctuations of individual recordings (Figure 5B). This  
210 effect is consistent with observation from previous figures: the amygdala showing both a  
211 relatively low-level of hyperemia during REMS compared to other regions (Figure 2) and low-  
212 correlation scores (Figure 3). Strikingly, the amygdala’s activity during REMS, showed a  
213 remarkably unique activation profile compared to the rest of the brain and long periods of  
214 strong fluctuation when the remainder of brain activity was silent (Figure 5B, second part of  
215 the episode). This effect was confirmed and strengthened using a seed-based approach taking  
216 either the regional whole-brain activity as a reference (Figure 5C, Supplementary Figure S4)  
217 or the amygdala (Figure 5D), which revealed are very strong and robust dissociation between  
218 the amygdala and all other brain regions. Interestingly, amygdala sub-structures seem to  
219 exhibit also very specific dynamics as shown by the heterogeneous correlation maps found by  
220 taking 5 different sub-regions (amygdalohippocampal area, posterolateral part: AHiPL,  
221 amygdalohippocampal area, posteromedial part: AHiPm, amygdalopiriform transition area:  
222 APir, basolateral amygdaloid nucleus, posterior part: BLP, posterolateral cortical amygdaloid  
223 nucleus: PLCo). These results suggest a strong dissociation between the amygdala and all  
224 other brain regions during specific epochs of REMS, but also among the amygdala itself.  
225

## 226 **Discussion**

227 This study provides a whole-brain characterization of the cerebral and vascular structures  
228 involved in the atypical and large-amplitude vascular surges occurring during REMS. This  
229 study goes significantly deeper in the understanding of REMS-associated hyperemia, as it  
230 imaged a very large number of brain regions (257 regions) over hundreds of REMS episodes.  
231 We implemented fUS imaging in 2D imaging planes with light ultrasonic probes as it is  
232 compatible with both unrestrained movement and naturally induced sleep studies. 2D fUS  
233 imaging enables us to ensure that the animal is not restrained, behaves almost perfectly  
234 normally, and sleeps spontaneously. It is primordial as stressed and head-restrained animals  
235 are less eager to sleep and deprivation protocols are often used to acquire sleep data, which  
236 affects both the structure and nature of sleep episodes. As each imaging session could only  
237 image on one single 2D plane, we had to repeat the experiment a large number of times in  
238 order to achieve an almost full 3D coverage of the brain’s regional activity during REMS.

239 Although this approach of multiple 2D planes has the disadvantage to lose the temporal  
240 information regarding the coactivity of brain regions from different planes, we solved this  
241 difficulty by imaging from both coronal and sagittal planes, thus relying on a respectable  
242 number of co-activated regions in each single session.

243 Although recent technological demonstrations of full 3D fUS imaging using piezo-electric  
244 matrix arrays (Brunner et al., 2020; Rabut et al., 2019) or Raw-Colum arrays (Sauvage et al.,  
245 2018, 2020) are very promising, they remain to date limited in use, as the heavy weight and  
246 limited sensitivity of these probes requires the animal to be head-fixed, thus rendering sleep  
247 studies unsuitable and further from normal behavior.

248 A previous study by our lab has unraveled an intense hyperemic activity during REMS, which  
249 largely exceeded both NREMS and wake levels (Bergel et al., 2018). This hyperemic state is  
250 decomposed in a tonic component (the elevation of the baseline) and in a phasic one which is  
251 robustly preceded by fast gamma oscillations in the CA1 region. This finding is striking as sleep  
252 is supposedly a state in which energy levels are reconstructed (Cirelli and Tononi, 2008;  
253 Schmidt, 2014; Siegel, 2005), yet this activity must be highly energy consuming. This  
254 hyperemic activity has been confirmed by more recent studies, using intrinsic optical imaging  
255 (ISOI) in sleeping head-fixed mice (Turner et al., 2020). However, most imaging modalities used  
256 so far for REMS studies are either focused on the cortical part or have such a limited temporal  
257 resolution that it impedes deeper fundamental understanding.

258 Such hyperemic activity might be physiologically important as it was kept throughout evolution,  
259 despite its energy consumption. Moreover, a clear picture of global brain activity during REMS  
260 is still currently missing.

261 In this study, we used functional ultrasound imaging to gather data on more than 250 brain  
262 regions in both coronal and sagittal planes, thus providing a very exhaustive characterization  
263 of global brain hemodynamics during rodent REMS. We demonstrate a clear dissociation  
264 between basal/midbrain structures and superficial ones, respectively activated in a tonic and  
265 phasic manner. We also disentangle the vascular structures involved in the irrigation of the  
266 brain during REMS episodes providing a detailed outlook of blood supply. Finally, one of the  
267 most noteworthy result of this work is the striking global dissociation of the amygdala activity  
268 from the rest of the brain during the REM episodes.

269

### 270 **Massive hyperemia observed across the whole brain and neurovascular coupling**

271 A previous study has already shown a hyperemic activity during REMS in humans in some  
272 brain regions in human using positron emission tomography (Maquet et al., 1996). However,  
273 this study only presented a higher vascular activity correlated with REMS in pontine

274 tegmentum, left thalamus, both amygdaloid complexes, anterior cingulate cortex and right  
275 parietal operculum, and some regions with a negative correlation with REMS mainly in cortical  
276 areas.

277 One of the key findings of the present work is that hyperemia is global and spans throughout  
278 all of the forebrain that we were able to image (2/3 of total brain volume). Additionally, it was  
279 more sustained in the deep/midbrain structures (in particular in the hippocampus) than in the  
280 cortex, which activated in phasic bouts. Thus, REMS can be described as a state of tonic  
281 hyperemia in the forebrain that only partially spreads to the cortex. Also, activity in the different  
282 cortices were strongly heterogeneous, with strongest activations in the retrosplenial, limbic,  
283 motor and visual cortices but close to the levels of wake in the other sensory cortices  
284 (somatosensory, piriform). This is surprising as rats preferentially use odor and texture rather  
285 than vision. Hence, it is possible that hyperemia is associated with the reactivation of visual  
286 networks (geniculate, colliculus, cortex) or in link with memory (retrosplenial, septum, and  
287 hippocampus). Vascular hyperactivity specific to REMS in rats divides into tonic and phasic  
288 regimes, the latter exhibiting transient brain-wide hyperemic patterns, which we called vascular  
289 surges (VS). Bergel et al showed that these VS outmatched wake levels occasionally reaching  
290 up to a 100% increase in the cortical and hippocampal regions compared to a quiet wake state.  
291 Precursors to VS in the theta (6–10 Hz) and high-gamma (70–110 Hz) bands of hippocampal  
292 LFP, and the intensity of each individual VS was best accounted for by the power of fast  
293 gamma, suggesting a strong association between local electrographic events and massive  
294 brain-wide vascular patterns. These VS exhibit a strong link with LFP gamma power in some  
295 brain structures (Bergel et al., 2018). Although a high correlation was already found in former  
296 fUS imaging studies between the fUS signal and EEG recordings (Mace et al., 2013; Nunez-  
297 Elizalde et al., 2021; Sieu et al., 2015) and neural calcium activity (Aydin et al., 2020) in  
298 accordance with the neurovascular coupling model (Iadecola, 2017), the massiveness of the  
299 hyperemia during REMS cannot be unambiguously linked to the sole neural activity. Such very  
300 high hyperemia may also partly be linked to the metabolic demand of other cell type cells such  
301 as glial cells or the drainage of the glymphatic system occurring during sleep (Plog and  
302 Nedergaard, 2018).

303

### 304 **Global dissociation of the amygdala and its substructures with the rest of the brain**

305 Though it is known that dreams occur during both NREMS and REMS (Stickgold et al., 1994),  
306 REMS ones are more vivid and intense, thus raising the assumed link between emotions and  
307 REMS. In “The Interpretation of Dreams” by Sigmund Freud, Freud focuses on the importance  
308 of dreams and their understanding, as he considered them to be the gate to one’s unconscious

309 and emotional state (Freud, Sigmund, 1900). More recent studies have confirmed this link  
310 between REMS and emotions such as the beneficial effect of sleep (and especially REMS) on  
311 negative emotions, and even a link between sleep disturbances and the lack of such beneficial  
312 effects (see for review (Vandekerckhove and Wang, 2017)). The “sleep to forget, sleep to  
313 remember” (SFSR) model (Walker and van der Helm, 2009) also points towards a role of  
314 REMS on the regulation of the emotional valence of memories, while the factual component is  
315 encoded in the hippocampus.

316 Recent research has further revealed the function of sleep in regulating emotion to be  
317 primordial (Baglioni et al., 2010). Considering the major link between REMS and the regulation  
318 of emotions, it is of particular interest to highlight here a strongly dissociated activity of the  
319 amygdala compared to the rest of the brain. Indeed, a higher vascular activity in amygdala was  
320 already found correlated with REMS using positron emission tomography in humans (Maquet  
321 et al., 1996). Interestingly, our results also indicate that this amygdala hyperemia presents a  
322 lower correlation with the rest of the brain regions, depicting a global dissociation of the  
323 amygdala from other brain regions.

324 The function of sleep in regulating emotion was found to be essential (Krause et al., 2017).  
325 REMS physiology was associated with an overnight dissipation of amygdala activity in  
326 response to previous emotional experiences, altering functional-connectivity and reducing  
327 next-day subjective emotionality (van der Helm et al., 2011). It is believed that during REMS  
328 and through several sleep sessions, high co-activation of hippocampus and amygdala will  
329 strengthen the consolidation of an emotional memory while downscaling its intensity (Walker  
330 and van der Helm, 2009). Then, once an aversive memory is triggered during wake, the  
331 hippocampus will send a cue to the mPFC to inhibit the amygdala, so that this 3-way switch  
332 supposedly downscales the emotional response to the memory. Finally, during REMS, bursts  
333 of PGO waves were also recorded across the pontine tegmentum to the geniculate nuclei of  
334 the thalamus and the occipital cortex in humans. These PGO waves have been linked with  
335 memory consolidation and they enhance synaptic plasticity in the amygdala and dorsal  
336 hippocampus (Datta et al., 2008). Rats also appear to produce PGO waves following direct  
337 electrical stimulation of the amygdala (Deboer et al., 1998). Such link is thought to indicate a  
338 relationship between dreaming and specific epochs of alertness (Gott et al., 2017). Further  
339 investigations into rats have revealed important links between the PGO waves and memory-  
340 related gene expression in both the amygdala and hippocampus (Datta et al., 2008), while  
341 another study has correlated PGO wave density with successful consolidation fear extinction  
342 following traumatic stress (Datta and O'Malley, 2013).

343 Moreover, it is known for many years that the amygdala is electrophysiologically active during  
344 REMS (White and Jacobs, 1975) and was also confirmed more recently during NREMS  
345 (Girardeau et al., 2017). Our hypothesis is that during REMS, while the amygdala is active, it  
346 is only strongly activated when the rest of the brain is not and especially the mPFC resulting  
347 in the lower correlation observed in the connectivity matrix. Rats might need to regularly go  
348 through phases of emotional regulation during REMS to cope with every day's accumulation  
349 of strong emotional memories.

350 We hypothesize that we image here this downscaling at play using functional ultrasound  
351 imaging during REMS. Finally, such a portable and wide field-of-view neuroimaging modality,  
352 as functional Ultrasound imaging provides an extensive picture of brain function and the  
353 interaction between large scale brain networks during sleep in rodents.

354

355

356 **Methods**

357 Animal Surgery

358 All animals received humane care in compliance with the European Communities Council  
359 Directive of 2010 (2010/63/EU). The experimental protocol used in this study was extensively  
360 reviewed and approved by the French CEEA (Comité Ethique pour l'Expérimentation Animale)  
361 n°59 Paris Centre et Sud under the reference number 2018061320381023. Adult Sprague  
362 Dawley rats aged 12-13 weeks were first put through a week of habituation with the  
363 experimenter and then underwent surgical craniotomy and implant of an ultrasound-clear  
364 prosthesis. Anesthesia was induced with 2% isoflurane and maintained with ketamine/xylazine  
365 (80/10 mg/kg), while body temperature was maintained at 37.0°C with a heating pad (Phymep,  
366 Paris, France). A sagittal skin incision was performed across the posterior part of the head to  
367 expose the skull. We excised the parietal and frontal flaps by drilling and gently moving the  
368 bone away from the dura mater. The opening exposed the brain from Bregma +4.0 to Bregma  
369 -9.0 mm, with a maximal width of 14 mm. An electrode was implanted stereotaxically and  
370 anchored on the edge of the flap. A prosthetic skull was sealed in place with acrylic resin (GC  
371 Unifast TRAD), and the residual space was filled with saline. We chose a prosthesis approach  
372 that offers a larger field of view and prolonged imaging condition over 4-6 weeks compared to  
373 the thinned bone approach. The prosthetic skull is composed of polymethylpentene  
374 (Goodfellow, Huntington UK, goodfellow.com), a standard biopolymer used for implants. This  
375 material has tissue-like acoustic impedance that allows undistorted propagation of ultrasound  
376 waves at the acoustic gel-prosthesis and prosthesis-saline interfaces. The prosthesis was cut  
377 out of a film of 250 µm thickness and permanently sealed to the skull. Particular care was  
378 taken not to tear the dura to prevent cerebral damage. The surgical procedure, including  
379 electrode implantation, typically took 6 hours. Animals were subcutaneously injected with anti-  
380 inflammatory drug (Metacam, 0.2 mg/kg) and prophylactic antibiotics (Borgal, 16mg/kg), and  
381 postoperative care was performed for 7 days. Animals recovered quickly and were used for  
382 data acquisition after a conservative one-week resting period.

383

384 Electrode design and implantation

385 Electrodes are based on linear polytrodes grouped in bundles of insulated tungsten wires. The  
386 difference with a standard design is a 90°-angle elbow that is formed prior to insertion in the  
387 brain<sup>44</sup>. This shape enabled anchoring of the electrode on the skull posterior to the flap. An  
388 electrode was implanted with stereotaxic positioning micromotion. The prosthesis was then  
389 applied to seal the skull. Four epidural screws placed above the cerebellum and above the  
390 olfactory bulbs were used as references and grounds. The intra-hippocampal handmade

391 electrode was composed of 25 to 50  $\mu\text{m}$  diameter insulated tungsten wires soldered to  
392 miniature connectors (Omnetics Inc, Minneapolis, US). Eight conductive ends were spaced  
393 0.5 to 1 mm apart and glued to form a 5.5 mm-long, 100-150- $\mu\text{m}$ -diameter bundle. The bundles  
394 were lowered in the dorsal hippocampus (left or right) at stereotaxic coordinates AP = -4.0 mm,  
395 ML = +/- 2.5 mm and DV = -1.5 mm to -4.5 mm relative to the Bregma. In addition to tungsten  
396 wires, we used copper wires (0.28 mm diameter) to measure the muscular activity  
397 (electromyogram EMG) in the neck muscles. Before each surgery, the relative position and  
398 distance between each recording site on the electrode (8 recording sites per electrode) was  
399 identified by measuring the impedance change, while lowering the electrodes in saline solution  
400 (Na-Cl 0.9%). The actual design was based on handmade electrodes with minimal spacing of  
401 500 microns between recording sites and a maximal number of 8 recording sites per electrode.  
402 This allows to observe the characteristic phase reversal between the superficial and deep  
403 layers of the dorsal hippocampus<sup>83</sup>, but not to quantify the cross-frequency coupling as with  
404 linear probes. Additionally, the surgical procedure is complex and there is variability between  
405 targeted structure and actual electrode position due to brain tissue movement (swelling) both  
406 during and after the surgery. See Supplementary Figure 1 for further details.

407

#### 408 Electrode implantation verification

409 Electrodes sites' locations were verified post mortem via histology to reconstruct the tract of  
410 electrode bundles in the tissue. Each rat was euthanized and perfused with paraformaldehyde  
411 4% to preserve the brains. Each brain was then cut using a vibratome to make 100 $\mu\text{m}$ -thick  
412 slices. The slices were then contrasted using hematoxyline/eosine coloration and scanned  
413 using a nanoscan. We then compared the slices with plates from Paxinos and defined the  
414 trajectory of implantation using the marks left by the electrode in the brain. Knowing the  
415 distances between the recording points, we could then define their position.

416

#### 417 Recording sessions

418 After a recovery week following the surgical procedure, the animals were fit to be used in data  
419 acquisition. After applying a generous amount of centrifuged ultrasonic gel, the ultrasonic  
420 probe was put in place using a magnetic probe holder (home-made 3D designed and printed)  
421 and the headstage for LFP recordings was plugged onto the connector. The animal was then  
422 placed inside a box under an infra-red camera (to monitor the behavior) and the data  
423 acquisition started. The ultrasonic probe was placed randomly across the day and its position  
424 was changed after 2-3 30 min-acquisitions. A typical recording session scanned 4 different  
425 brain plans and lasted approximately 6 hours with different breaks. All the probe and

426 headstage positioning and moving was realized without having to put the animal under  
427 anesthesia. At the end of the recording session, the window is cleaned from excess ultrasonic  
428 gel and the animal is replaced in its home-cage.

429

430

#### 431 LFP acquisition

432 LFP, electromyogram (EMG) and accelerometer (ACC) signals and video were monitored  
433 continuously from video-EEG device for offline processing. Intracranial electrode signals were  
434 fed through a Blackrock Cereplex System using the Cereplex Direct Software Suite (version  
435 7.0.6.0) developed by Blackrock Microsystems (Salt Lake City, UT, USA), together with a  
436 synchronization signal from the ultrasound scanner. LFP signals were pre-amplified and  
437 digitized onto the animal's head which prevent artifacts originating from cable movement. A  
438 regular amplifier was used, and no additional electronic circuit for artifact suppression was  
439 necessary. A large bandwidth amplifier was used, which can record local field potentials in all  
440 physiological bands (LFP, 0.1-2 kHz). The spatial resolution of LFPs ranges from 250  $\mu\text{m}$  to a  
441 few mm radius.

442

#### 443 Ultrasound Acquisition

444 Vascular images were obtained via the ultrafast compound Doppler imaging technique<sup>84</sup>. The  
445 probe was driven by a fully programmable GPU-based ultrafast ultrasound scanner Verasonics  
446 (Kirkland, USA), relying on 24-Gb RAM memory. We continuously acquired  $N=4500$  Doppler  
447 ultrasound images at 2.5 Hz frame rate for 30 minutes straight. Each Doppler frame is obtained  
448 using the accumulation of 100 successive compound plane-wave frames, each compounded  
449 frame corresponding to a coherent summation of beamformed complex in phase/quadrature  
450 (IQ) images obtained from the insonification of the medium with a set of successive plane  
451 waves with specific tilting angles<sup>85</sup>. Given the tradeoff between frame rate, resolution and  
452 imaging speed, a plane-wave compounding using eight  $2^\circ$ -apart angles of insonification (from  
453  $-7^\circ$  to  $+7^\circ$ ) was chosen. As a result, the pulse repetition frequency of the plane wave  
454 transmissions was 4000 Hz. To discriminate blood signals from tissue clutter, the ultrafast  
455 compound Doppler frame stack was filtered, removing the 60 first components of the singular  
456 value decomposition, which optimally exploited the spatiotemporal dynamics of the full Doppler  
457 film for clutter rejection, largely outperforming conventional clutter rejection filters used in  
458 Doppler ultrasound<sup>86</sup>.

459

#### 460 LFP analysis

461 All analysis was performed in MATLAB (version R2017b, Mathworks, USA). NPMK package  
462 (version 4.5.3.0) developed by Blackrock Microsystems was used to import the raw LFP data  
463 into MATLAB. EEG was collected and high-pass filtered above 250 Hz. This, together with  
464 direct amplification onto the animal's head via the INTAN chip from the Blackrock system,  
465 allows for quality and artifact-free LFP recording in the motor cortex and hippocampus during  
466 free running. EEG was then band-pass filtered in typical frequency bands including delta (1-4  
467 Hz), theta (4-10 Hz), beta (10-20 Hz), low-gamma (20-50 Hz), mid-gamma (50-100 Hz), upper  
468 mid-gamma (80-120 Hz), high-gamma (100-150 Hz), upper high-gamma (130-180 Hz) and  
469 ripple (150-250 Hz). This division has been thoroughly described and proven to be functionally  
470 relevant for hippocampal electrographic recordings<sup>50</sup>.

471

#### 472 Sleep scoring

473 Signals from the EMG, ACC and LFP recordings were used to perform the sleep scoring. It  
474 allowed us to separate four different vigilance states: active wake (AW), quiet wake (QW), REM  
475 sleep (REMS) and non-REM sleep (NREMS). Each of these states is characterized by a  
476 combination of indexes drawn from the recorded signals. We computed the power of the EMG  
477 signal (as used in Katsageorgiou et al. 2015), the ratio theta/delta of the LFP signal and then  
478 manually thresholded these two parameters and the accelerometer signal to obtain indexes  
479 made of zeros and ones. The four different vigilance states are defined thus: AW = EMG 1 +  
480 ACC 1 + ratio 0/1; QW = EMG 1 + ACC 0 + ratio 0/1; REM = EMG 0 + ACC 0 + ratio 1; NREMS  
481 = EMG 0 + ACC 0 + ratio 0. Video was used from time to time to confirm the sleep scoring.

482

#### 483 CBV maps & spatial averaging

484 Previous studies from our group have shown that the fUS signal tightly relates to neuronal  
485 activity and microscopic single-vessel hemodynamics. In order to build the CBV maps from  
486 the raw back-scattered echoes, radiofrequency (RF) signals are delayed and summed to form  
487 IQ matrices through a process known as beamforming. These matrices are then decomposed  
488 via Singular Value Decomposition (SVD) to decouple slow movements due to pulsatility and  
489 tissue motion from fast movements due to echogenic particles crossing a voxel during a full  
490 cardiac cycle (200 milliseconds). Importantly, Power Doppler images are computed by taking  
491 the power of the full Doppler spectrum, including a range of speeds in large and smaller  
492 vessels, with a typical inferior bound of 2-5 mm/s in axial velocity. This gives a signal  
493 proportional to the number of echogenic particles that have crossed a single voxel during 200  
494 milliseconds (with a sufficient axial velocity) which is a good estimate of local cerebral blood  
495 flow (CBF). We thus can build Doppler movies with a sampling frequency of 2.5 Hz, which can

496 even be increased if needed up to the pulse repetition frequency (here 500 Hz) through the  
497 use of a temporal sliding window. To derive CBV maps from the raw Doppler movies, we  
498 performed voxel-wise normalization from a baseline period: depending on the analysis done  
499 afterwards, we either used 2 minutes of quiet wake, 2 mins of active wake, or the 20 seconds  
500 preceding the onset of a REM episode. We extracted the distribution for each voxel during this  
501 baseline period and computed a mean value, leading to one value for each voxel of the image.  
502 To derive a signal similar to  $\Delta F/F$  in fluorescence microscopy, we subtracted the mean and  
503 divided by the mean for each voxel in the Doppler movie. This allowed normalization and  
504 rescaling of ultrasound data, yielding to an expression in terms of percent of variation relative  
505 to baseline (CBV % change). Each voxel was normalized independently before performing  
506 spatial averaging.

507

#### 508 Atlas registration

509 Coronal recordings were registered to two-dimensional sections from the Paxinos atlas  
510 (Paxinos and Watson, 2017) using anatomical landmarks, such as cortex edges, hippocampus  
511 outer shape and large vessels below brain surface as a reference. We performed manual  
512 scaling and rotation along each of the 3 dimensions to recover the most probable registration.  
513 Once performed, regions of interest were extracted using binary masks. This process allowed  
514 us to derive vascular activity in 259 brain regions.

515

#### 516 Cross-correlation analysis

517 We used Pearson's cross-correlation score to quantify the association between REM episodes  
518 and the CBV activations in brain regions, or between brain regions, or between LFP signals  
519 and CBV activations in brain regions. To do so, we performed the cross-correlation  
520 computation on a large temporal window, depending on the couple analyzed. Regarding the  
521 CBV activations, we either used pixels (Fig. 5 C-E) or averaged values over brain regions or  
522 structures.

523

#### 524 LFP-CBV correlation analysis

525 To assess the association between LFP events and CBV variables, we searched for  
526 correlations between each possible combination of LFP band-pass filtered signals and regional  
527 CBV variables. As neurovascular processes are not instantaneous, we considered possible  
528 delays between electrographic and vascular signals and thus computed cross-correlations  
529 functions between the two signals for any LFP-CBV pair and any lag in a given time window (-

530 1.0 s to 5.0 s). We performed this analysis over pixel and regional variables, but only regional  
531 variables allowed for statistical comparison across recordings.

532

### 533 Identification of vascular structures

534 Another technical difficulty we encountered was the recognition of the imaging planes /  
535 registrations of these planes in a 3D map. Our laboratory recently developed such approach  
536 in mice, by co-registering a vascular atlas on the atlas from the Allen Brain Institute (Nouhoum  
537 et al., 2021). Such Approach will be available in the near future for rats, using recently  
538 published vascular and MRI atlas in rats. But at the time of these experiments, this was not  
539 available. Instead we used the few vascular atlas currently available in rats and mice (Scremin,  
540 2015; Xiong et al., 2017) and in particular imaging plane, we performed Ultrasound  
541 Localisation Microscopy. This technique enables, through the detection and tracking of  
542 individual micro-bubbles injected intravenously that constitute contrast agents (Errico et al.,  
543 2015), to visualize the vasculature with a higher sensitivity and contrast, but also to measure  
544 the direction and speed of blood flow at a microscopic scale in both rodents (Errico et al., 2015)  
545 and human (Demené et al., 2021).

546

547

### 548 Statistics and Reproducibility

549 All statistics are given as +/- standard error of the mean, unless stated otherwise. Statistics in  
550 Fig. 3 are computed on n=11 animals over 42 recording sessions. Bar diagrams shown in Fig.  
551 3 are computed by averaging the mean values of 22 recordings on 11 animals for the coronal  
552 planes and 20 recordings in 7 animals for the diagonal planes. Statistics are computed using  
553 a two-tailed Mann-Whitney test. The significance of Pearson correlation coefficients shown in  
554 Fig. 3 and Fig. 7 are assessed by computing the t-value (using  $t = \frac{r\sqrt{1-r^2}}{\sqrt{n-2}}$ ) and reporting it in  
555 Student's table with n-2 degrees of freedom. Statistical testing for correlation distributions were  
556 computed after Fischer transformation. Multiple comparison for regional analyses were  
557 accounted for using Bonferroni correction. Due to the difficult experimental constraints (difficult  
558 surgical procedure, precise electrode implantation, habituation and training required for the  
559 locomotion task) no replication attempt was performed in this study, but the results were robust  
560 and observable across individuals and recordings.

561 **References**

- 562 Aydin, A.-K., Haselden, W.D., Goulam Houssen, Y., Pouzat, C., Rungta, R.L., Demené, C.,  
563 Tanter, M., Drew, P.J., Charpak, S., and Boido, D. (2020). Transfer functions linking neural  
564 calcium to single voxel functional ultrasound signal. *Nat Commun* 11, 2954.
- 565 Baglioni, C., Spiegelhalter, K., Lombardo, C., and Riemann, D. (2010). Sleep and emotions:  
566 A focus on insomnia. *Sleep Medicine Reviews* 14, 227–238.
- 567 Bergel, A., Deffieux, T., Demené, C., Tanter, M., and Cohen, I. (2018). Local hippocampal fast  
568 gamma rhythms precede brain-wide hyperemic patterns during spontaneous rodent REM sleep.  
569 *Nature Communications* 9, 5364.
- 570 Blumberg, M.S., Coleman, C.M., Gerth, A.I., and McMurray, B. (2013). Spatiotemporal  
571 Structure of REM Sleep Twitching Reveals Developmental Origins of Motor Synergies.  
572 *Current Biology* 23, 2100–2109.
- 573 Bottary, R., Seo, J., Daffre, C., Gazecki, S., Moore, K.N., Kopotiyenko, K., Dominguez, J.P.,  
574 Gannon, K., Lasko, N.B., Roth, B., et al. (2020). Fear extinction memory is negatively  
575 associated with REM sleep in insomnia disorder. *Sleep* 43, zsa007.
- 576 Boyce, R., Glasgow, S.D., Williams, S., and Adamantidis, A. (2016). Causal evidence for the  
577 role of REM sleep theta rhythm in contextual memory consolidation. *Science* 352, 812–816.
- 578 Brunner, C., Grillet, M., Sans-Dublanc, A., Farrow, K., Lambert, T., Macé, E., Montaldo, G.,  
579 and Urban, A. (2020). A Platform for Brain-wide Volumetric Functional Ultrasound Imaging  
580 and Analysis of Circuit Dynamics in Awake Mice. *Neuron* 108, 861-875.e7.
- 581 Chow, H.M., Horovitz, S.G., Carr, W.S., Picchioni, D., Coddington, N., Fukunaga, M., Xu, Y.,  
582 Balkin, T.J., Duyn, J.H., and Braun, A.R. (2013). Rhythmic alternating patterns of brain activity  
583 distinguish rapid eye movement sleep from other states of consciousness. *Proceedings of the*  
584 *National Academy of Sciences* 110, 10300–10305.
- 585 Cirelli, C., and Tononi, G. (2008). Is Sleep Essential? *PLOS Biology* 6, e216.
- 586 Datta, S., and O'Malley, M.W. (2013). Fear Extinction Memory Consolidation Requires  
587 Potentiation of Pontine-Wave Activity during REM Sleep. *Journal of Neuroscience* 33, 4561–  
588 4569.
- 589 Datta, S., Li, G., and Auerbach, S. (2008). Activation of phasic pontine-wave generator in the  
590 rat: a mechanism for expression of plasticity-related genes and proteins in the dorsal  
591 hippocampus and amygdala. *European Journal of Neuroscience* 27, 1876–1892.

592 Deboer, T., Sanford, L.D., Ross, R.J., and Morrison, A.R. (1998). Effects of electrical  
593 stimulation in the amygdala on ponto-geniculo-occipital waves in rats. *Brain Research* 793,  
594 305–310.

595 Demene, C., Baranger, J., Bernal, M., Delanoe, C., Auvin, S., Biran, V., Alison, M., Mairesse,  
596 J., Harribaud, E., Pernot, M., et al. (2017). Functional ultrasound imaging of brain activity in  
597 human newborns. *Science Translational Medicine* 9, eaah6756.

598 Demené, C., Robin, J., Dizeux, A., Heiles, B., Pernot, M., Tanter, M., and Perren, F. (2021).  
599 Transcranial ultrafast ultrasound localization microscopy of brain vasculature in patients. *Nat*  
600 *Biomed Eng* 5, 219–228.

601 Errico, C., Pierre, J., Pezet, S., Desailly, Y., Lenkei, Z., Couture, O., and Tanter, M. (2015).  
602 Ultrafast ultrasound localization microscopy for deep super-resolution vascular imaging.  
603 *Nature* 527, 499–502.

604 Freud, Sigmund (1900). *The Interpretation of Dreams*.

605 Girardeau, G., Inema, I., and Buzsáki, G. (2017). Reactivations of emotional memory in the  
606 hippocampus–amygdala system during sleep. *Nat Neurosci* 20, 1634–1642.

607 Gott, J.A., Liley, D.T.J., and Hobson, J.A. (2017). Towards a Functional Understanding of PGO  
608 Waves. *Frontiers in Human Neuroscience* 11, 89.

609 Groch, S., Zinke, K., Wilhelm, I., and Born, J. (2015). Dissociating the contributions of slow-  
610 wave sleep and rapid eye movement sleep to emotional item and source memory. *Neurobiology*  
611 *of Learning and Memory* 122, 122–130.

612 Grosmark, A.D., Mizuseki, K., Pastalkova, E., Diba, K., and Buzsáki, G. (2012). REM Sleep  
613 Reorganizes Hippocampal Excitability. *Neuron* 75, 1001–1007.

614 Gujar, N., McDonald, S.A., Nishida, M., and Walker, M.P. (2011). A Role for REM Sleep in  
615 Recalibrating the Sensitivity of the Human Brain to Specific Emotions. *Cerebral Cortex* 21,  
616 115–123.

617 Hutchison, I.C., and Rathore, S. (2015). The role of REM sleep theta activity in emotional  
618 memory. *Front Psychol* 6, 1439.

619 Iadecola, C. (2017). The Neurovascular Unit Coming of Age: A Journey through Neurovascular  
620 Coupling in Health and Disease. *Neuron* 96, 17–42.

621 Izawa, S., Chowdhury, S., Miyazaki, T., Mukai, Y., Ono, D., Inoue, R., Ohmura, Y.,  
622 Mizoguchi, H., Kimura, K., Yoshioka, M., et al. (2019). REM sleep–active MCH neurons are  
623 involved in forgetting hippocampus-dependent memories. *Science* 365, 1308–1313.

624 Krause, A.J., Simon, E.B., Mander, B.A., Greer, S.M., Saletin, J.M., Goldstein-Piekarski, A.N.,  
625 and Walker, M.P. (2017). The sleep-deprived human brain. *Nat Rev Neurosci* 18, 404–418.

626 Langille, J.J. (2019). Remembering to Forget: A Dual Role for Sleep Oscillations in Memory  
627 Consolidation and Forgetting. *Frontiers in Cellular Neuroscience* 13, 71.

628 Mace, E., Montaldo, G., Osmanski, B.F., Cohen, I., Fink, M., and Tanter, M. (2013). Functional  
629 ultrasound imaging of the brain: theory and basic principles. *IEEE Transactions on Ultrasonics,*  
630 *Ferroelectrics, and Frequency Control* 60, 492–506.

631 Maquet, P., Péters, J.-M., Aerts, J., Delfiore, G., Degueldre, C., Luxen, A., and Franck, G.  
632 (1996). Functional neuroanatomy of human rapid-eye-movement sleep and dreaming. *Nature*  
633 383, 163–166.

634 Marks, G.A., Shaffery, J.P., Oksenberg, A., Speciale, S.G., and Roffwarg, H.P. (1995). A  
635 functional role for REM sleep in brain maturation. *Behavioural Brain Research* 69, 1–11.

636 Mateo, C., Knutsen, P.M., Tsai, P.S., Shih, A.Y., and Kleinfeld, D. (2017). Entrainment of  
637 Arteriole Vasomotor Fluctuations by Neural Activity Is a Basis of Blood-Oxygenation-Level-  
638 Dependent “Resting-State” Connectivity. *Neuron* 96, 936-948.e3.

639 Mellman, T.A., Bustamante, V., Fins, A.I., Pigeon, W.R., and Nolan, B. (2002). REM Sleep  
640 and the Early Development of Posttraumatic Stress Disorder. *AJP* 159, 1696–1701.

641 Montgomery, S.M., Sirota, A., and Buzsaki, G. (2008). Theta and Gamma Coordination of  
642 Hippocampal Networks during Waking and Rapid Eye Movement Sleep. *Journal of*  
643 *Neuroscience* 28, 6731–6741.

644 Nishida, M., Pearsall, J., Buckner, R.L., and Walker, M.P. (2009). REM Sleep, Prefrontal  
645 Theta, and the Consolidation of Human Emotional Memory. *Cerebral Cortex* 19, 1158–1166.

646 Nouhoum, M., Ferrier, J., Osmanski, B.-F., Ialy-Radio, N., Pezet, S., Tanter, M., and Deffieux,  
647 T. (2021). A functional ultrasound brain GPS for automatic vascular-based neuronavigation.  
648 *Sci Rep* 11, 15197.

649 Nunez-Elizalde, A.O., Krumin, M., Reddy, C.B., Montaldo, G., Urban, A., Harris, K.D., and  
650 Carandini, M. (2021). Neural basis of functional ultrasound signals.

651 Pace-Schott, E.F., Germain, A., and Milad, M.R. (2015). Sleep and REM sleep disturbance in  
652 the pathophysiology of PTSD: the role of extinction memory. *Biol Mood Anxiety Disord* 5, 3.

653 Paxinos, G., and Watson, C. (2017). *The Rat Brain in Stereotaxic Coordinates: Compact*  
654 (Academic Press).

655 Peever, J., and Fuller, P.M. (2017). The Biology of REM Sleep. *Current Biology* 27, R1237–  
656 R1248.

657 Phelps, E.A. (2004). Human emotion and memory: interactions of the amygdala and  
658 hippocampal complex. *Current Opinion in Neurobiology* 14, 198–202.

659 Plog, B.A., and Nedergaard, M. (2018). The Glymphatic System in Central Nervous System  
660 Health and Disease: Past, Present, and Future. *Annual Review of Pathology: Mechanisms of*  
661 *Disease* 13, 379–394.

662 Popa, D., Duvarci, S., Popescu, A.T., Lena, C., and Pare, D. (2010). Coherent amygdalocortical  
663 theta promotes fear memory consolidation during paradoxical sleep. *Proceedings of the*  
664 *National Academy of Sciences* 107, 6516–6519.

665 Rabut, C., Correia, M., Finel, V., Pezet, S., Pernot, M., Deffieux, T., and Tanter, M. (2019). 4D  
666 functional ultrasound imaging of whole-brain activity in rodents. *Nat Methods* 16, 994–997.

667 Sastre, P.J.-P., and Jouvet, M. (1979). Le comportement onirique du chat. *Physiology &*  
668 *Behavior* 22, 979–989.

669 Sauvage, J., Flesch, M., Férin, G., Nguyen-Dinh, A., Porée, J., Tanter, M., Pernot, M., and  
670 Deffieux, T. (2018). A large aperture row column addressed probe for in vivo 4D ultrafast  
671 doppler ultrasound imaging. *Phys. Med. Biol.* 63, 215012.

672 Sauvage, J., Porée, J., Rabut, C., Férin, G., Flesch, M., Rosinski, B., Nguyen-Dinh, A., Tanter,  
673 M., Pernot, M., and Deffieux, T. (2020). 4D Functional Imaging of the Rat Brain Using a Large  
674 Aperture Row-Column Array. *IEEE Transactions on Medical Imaging* 39, 1884–1893.

675 Schmidt, M.H. (2014). The energy allocation function of sleep: A unifying theory of sleep,  
676 torpor, and continuous wakefulness. *Neuroscience & Biobehavioral Reviews* 47, 122–153.

677 Scremin, O.U. (2015). Chapter 31 - Cerebral Vascular System. In *The Rat Nervous System*  
678 (Fourth Edition), G. Paxinos, ed. (San Diego: Academic Press), pp. 985–1011.

679 Siegel, J.M. (2005). Clues to the functions of mammalian sleep. *Nature* 437, 1264–1271.

680 Sieu, L.-A., Bergel, A., Tiran, E., Deffieux, T., Pernot, M., Gennisson, J.-L., Tanter, M., and  
681 Cohen, I. (2015). EEG and functional ultrasound imaging in mobile rats. *Nature Methods* 12,  
682 831–834.

683 Spoormaker, V.I. (2018). PTSD, Arousal, and Disrupted (REM) Sleep. In *Sleep and Combat-*  
684 *Related Post Traumatic Stress Disorder*, E. Vermetten, A. Germain, and T.C. Neylan, eds. (New  
685 York, NY: Springer New York), pp. 227–232.

686 Stickgold, R., Pace-Schott, E., and Hobson, J.A. (1994). A New Paradigm for Dream Research:  
687 Mentation Reports Following Spontaneous Arousal from REM and NREM Sleep Recorded in  
688 a Home Setting. *Consciousness and Cognition* 3, 16–29.

689 Turner, K.L., Gheres, K.W., Proctor, E.A., and Drew, P.J. (2020). Neurovascular coupling and  
690 bilateral connectivity during NREM and REM sleep. *ELife* 9, e62071.

691 Vandekerckhove, M., and Wang, Y. (2017). Emotion, emotion regulation and sleep: An  
692 intimate relationship. *AIMS Neurosci* 5, 1–17.

693 van der Helm, E., Yao, J., Dutt, S., Rao, V., Saletin, J.M., and Walker, M.P. (2011). REM Sleep  
694 Depotentiates Amygdala Activity to Previous Emotional Experiences. *Current Biology* 21,  
695 2029–2032.

696 Vetrivelan, R., Kong, D., Ferrari, L.L., Arrigoni, E., Madara, J.C., Bandaru, S.S., Lowell, B.B.,  
697 Lu, J., and Saper, C.B. (2016). Melanin-concentrating hormone neurons specifically promote  
698 rapid eye movement sleep in mice. *Neuroscience* 336, 102–113.

699 Wagner, U., Gais, S., and Born, J. (2001). Emotional Memory Formation Is Enhanced across  
700 Sleep Intervals with High Amounts of Rapid Eye Movement Sleep. *Learn. Mem.* 8, 112–119.

701 Walker, M.P., and van der Helm, E. (2009). Overnight therapy? The role of sleep in emotional  
702 brain processing. *Psychol Bull* 135, 731–748.

703 Wehrle, R., Kaufmann, C., Wetter, T.C., Holsboer, F., Auer, D.P., Pollmächer, T., and Czisch,  
704 M. (2007). Functional microstates within human REM sleep: first evidence from fMRI of a  
705 thalamocortical network specific for phasic REM periods. *European Journal of Neuroscience*  
706 25, 863–871.

707 White, T.J., and Jacobs, B.L. (1975). Single unit activity in the lateral amygdala of the cat  
708 during sleep and waking. *Electroencephalography and Clinical Neurophysiology* 38, 331–333.

709 Wiesner, C.D., Pulst, J., Krause, F., Elsner, M., Baving, L., Pedersen, A., Prehn-Kristensen, A.,  
710 and Göder, R. (2015). The effect of selective REM-sleep deprivation on the consolidation and  
711 affective evaluation of emotional memories. *Neurobiology of Learning and Memory* 122, 131–  
712 141.

713 Xiong, B., Li, A., Lou, Y., Chen, S., Long, B., Peng, J., Yang, Z., Xu, T., Yang, X., Li, X., et  
714 al. (2017). Precise Cerebral Vascular Atlas in Stereotaxic Coordinates of Whole Mouse Brain.  
715 *Front. Neuroanat.* 11, 128.

716

717 **Acknowledgements**

718 The authors would like to thank F. Segura, M. Nouhoum, H. Serroune, A. Bertolo for their help  
719 in the different steps of the research leading to these results. The authors would also like to  
720 thank Dr. Isabelle Arnulf and Dr. Karim Benchenane for their fruitful scientific discussions and  
721 advices. The research leading to these results has received funding from the AXA Research  
722 Fund under the chair *New hopes in medical imaging with ultrasound*.

723 **Author contributions**

724 A.B. and M.T. designed the experiment. A.B. designed the electrodes and performed the  
725 surgeries. M.M. crafted the electrodes, performed the training and recording sessions. A.B.  
726 programmed the software for multimodal data visualization and analysis. A.B. and M.M  
727 analyzed the behavioral, electrographic data, and ultrasound data. M.M. and S.P. performed  
728 ULM experiments and identified vascular structures. All authors discussed multimodal  
729 analysis. All authors wrote the paper.

730 **Data availability**

731 All data and software supporting the findings of this study are available from the corresponding  
732 authors upon reasonable request. Custom codes used for the collection of fUS data are  
733 protected by Inserm and can only be shared upon request, with the written agreement of  
734 Inserm.

735 **Code availability**

736 The code used to generate the results that are reported in this study is available from the  
737 corresponding authors upon reasonable request. Custom codes used for the analysis of  
738 fUS/LFP/video data used in this study are protected by Inserm and can only be shared upon  
739 request, with the written agreement of Inserm.

740 **Competing interests**

741 The Authors declare the following competing interests: M.T. is co-founder and shareholder in  
742 the ICONEUS company.

743 **Materials & Correspondence**

744 Correspondence should be addressed to M.T ([mickael.tanter@espci.fr](mailto:mickael.tanter@espci.fr))



# Figures

## Figure 1

See image above for figure legend.

## Figure 2

See image above for figure legend.

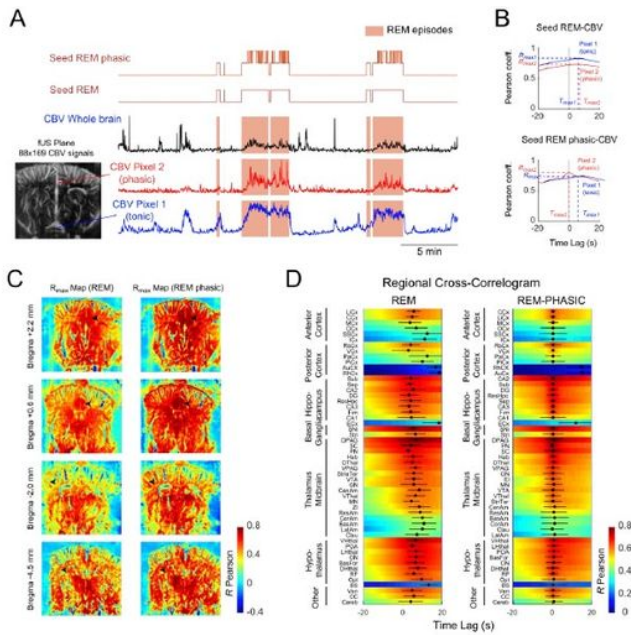


**Figure 3: Topological dissociation between tonic activation in the basal brain and phasic activation in the superficial brain areas**

(A) (Top) Typical fUS image (bottom left), seed variables (upper right) and CBV traces (right) in the whole brain (black) and two different voxels (blue: anterior cerebral artery, red: cingulate cortex) during a typical fUS recording. REMS episodes are denoted by shaded boxes. Note the difference in CBV dynamics between the basal and superficial voxels, showing respectively tonic (voxel 1, blue) and phasic (voxel 2) profiles. These are displayed concurrently with REMS "seed" variable (equals 1 during REM sleep, 0 otherwise) and REM-PHASIC seed (equals 2 during phasic REM sleep, 1 during non-phasic REM sleep, 0 otherwise). (B) Cross-correlation functions between the two seed variables and the two voxel CBV traces. The coordinates of the peak ( $T_{max}$ ,  $F_{max}$ ) were extracted and used as a measure of the coupling strength between the CBV variable and associated state (C) Maximal Correlation ( $R_{max}$ ) maps obtained by performing similar correlation analysis between the two seed variables and all CBV voxels traces in 4 different recording planes in one representative example (at Bregma +2.0 mm, +0.6 mm, -2.0 mm and -4.5 mm). Note how superficial voxels display stronger correlation in the

REMS-phasic map than REM maps, suggesting that they track phasic activations better than deep voxels (black arrows) (D) Mean cross-correlation functions computed for the whole set of acquisitions, sorted in decreasing correlation strength by region, for the REMS seed (left) and REMS-phasic seed (right). Hippocampal, midbrain and hypothalamus structures display the strongest coefficient for both analyses with the highest scores for the periaqueductal grey, the substantia nigra and the superior colliculus. Note the dispersion in time lags in the REMS analysis showing that regions are not activated at the same time, as well as the smaller  $T_{max}$  values in the REMS-phasic analysis centered on zero-lag, similar as in (B). Acronyms of the brain areas: see legend figure 2.

## Figure 3

See image above for figure legend.

## Figure 4

See image above for figure legend.

## Figure 5

See image above for figure legend.

## Supplementary Files

This is a list of supplementary files associated with this preprint. Click to download.

- [MateietalSupplementalFiguresandTables.pdf](#)